VTT Technical Research Centre of Finland

Modelling the effect of macro-segregation on the fracture toughness of heavy forgings using FFT based crystal plasticity simulations

Ren, Sicong C.; Marini, Bernard; Forget, Pierre

Published in:
Engineering Fracture Mechanics

DOI:
10.1016/j.engfracmech.2022.108694

Published: 01/09/2022

Document Version
Publisher's final version

Engineering Fracture Mechanics 272 (2022) 108694

Contents lists available at ScienceDirect

Engineering Fracture Mechanics

journal homepage: www.elsevier.com/locate/engfracmech

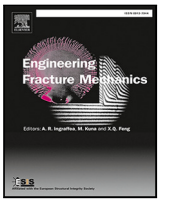

Modelling the effect of macro-segregation on the fracture toughness of heavy forgings using FFT based crystal plasticity simulations

S.C. Ren [a,b,*], B. Marini [a,*], P. Forget [a,*]

[a] Université Paris-Saclay, CEA, Service de Recherches Métallurgiques Appliquées, 91191, Gif-sur-Yvette, France
[b] VTT Technical Research Centre of Finland, P.O. Box 1000, FI-02044 VTT Espoo, Finland

ARTICLE INFO

Keywords:
Crystal plasticity
Macro-segregation
FFT method
Cleavage
Fracture toughness

ABSTRACT

The local approach has been successful in evaluating the brittle fracture probability of nuclear pressure vessel steels by establishing a link between microstructural defects and the macroscopic fracture behaviour. The evaluation of fracture probabilities relies on the applied stress on the smallest representative elementary volume. A proper description of the stress heterogeneities in polycrystals helps refine the prediction. The current work investigates the effect of carbon macro-segregation in heavy forgings and demonstrates a workflow combining crystal plasticity with the Microstructure Informed Brittle Fracture (MIBF) local approach model in fracture toughness prediction. The microstructural and mechanical properties of low alloy steels with different segregation levels were evaluated. A dislocation-density based crystal plasticity model which contains carbide strengthening contribution was identified and applied for modelling microstructure influence on local stress distributions. Results show that the microstructural evolution observed at high carbon levels has a significant influence on local stress distributions, which in turn affects the fracture toughness. The simulation results also demonstrate that, with proper input of microstructural information, the MIBF model is capable to predict the shift of the brittle-to-ductile transition zone with the variation of carbon and alloying elements and gives insights about factors affecting the resistance of materials.

1. Introduction

The embrittlement of reactor pressure vessel (RPV) steel has long been a concern of the nuclear industry. Fracture initiation is generally considered to occur on small defects nucleated on carbides. During the heavy forging fabrication process, macro-segregated areas of carbon, alloy elements and impurities are observed and could not be removed completely. These chemical heterogeneities can lead to significant variations in fracture toughness in the Ductile to Brittle Transition (DBT) regime [1,2].

Large scatter in measured brittle fracture toughness values is observed owing to the complexity of the microstructure. The development of the 'local approach' to fracture made it possible to establish a link between fracture toughness and local brittle fracture initiators [3–5]. A more recent review can be found in [6]. By introducing a notion of probability, the local approach provides physical explanations for the scatter of fracture toughness. The original version of the well known Beremin model attributes the scatter and specimen size effect in fracture toughness measurements to the distribution of carbide sizes. Following this work, most local approach models rely on carbides as crack initiators. Other microstructural sources causing scatter have also been discussed in literature, such as lath packets boundaries, cluster of manganese sulphide (MnS) inclusions [7–11] or the random distribution of the locations of cleavage sites [12].

* Corresponding authors.
E-mail addresses: sicong.ren@vtt.fi (S.C. Ren), bernard.marini@cea.fr (B. Marini), pierre.forget@cea.fr (P. Forget).

https://doi.org/10.1016/j.engfracmech.2022.108694
Received 26 April 2022; Received in revised form 5 July 2022; Accepted 31 July 2022
Available online 4 August 2022

Nomenclature

Acronyms

BCC	Body Centred Cubic
DBT	Ductile to Brittle Transition
$EBSD$	Electron Backscatter Diffraction
FFT	Fast Fourier Transform
HZ	Hard Zone
$MIBF$	Microstructure Informed Brittle Fracture
REV	Representative Elementary Volume
RPV	Reactor Pressure Vessel
SZ	Soft Zone

Greek characters

β_m	Scale parameter of Weibull distribution (stress)
α^s	Average obstacle strength on system s
α_{carb}	Shape parameter of Weibull distribution (carbide size distribution)
α_m	Shape parameter of Weibull distribution (stress)
β_{carb}	Scale parameter of Weibull distribution (carbide size distribution)
ΔG_0	Reference slip activation energy
$\dot{\rho}^s_{dis}$	Dislocation density rate
$\dot{\gamma}^s$	Slip rate of system s
$\dot{\gamma}^s_{drag}$	Jog-drag driven slip rate
$\dot{\gamma}^s_{friction}$	Lattice friction driven slip rate
$\dot{\gamma}_0$	Reference shear rate
η	Stress triaxiality
γ_{carb}	Location parameter of Weibull distribution (carbide size distribution)
γ_f	Effective fracture surface energy
γ_m	Location parameter of Weibull distribution (stress)
Λ^s	Dislocation mean free path
λ^s	Average obstacle spacing
$\left\langle \sigma_{V_0 I} \right\rangle$	Average maximum principal stress applied on each V_0
μ	Shear modulus
μ_{300K}	Shear modulus at 300 K
ρ^s_m	Mobile dislocation density
ρ^s_{carb}	Carbide density
ρ^s_{dis}	Dislocation density
ρ^s_{obs}	Total obstacle density
ρ^s_{ref}	Reference forest dislocation density
σ_c	Critical fracture stress
τ^s	Resolved shear stress
τ^s_c	Critical resolved shear stress
τ^s_{HP}	Hall–Petch effect induced stress
τ^s_{LT}	Line tension induced stress
τ^s_{self}	Self-interaction induced stress
τ_0	Critical resolved shear stress of Fe single crystal
τ^s_{eff}	Effective shear stress

Latin characters

$\langle P_1 \rangle$	Average maximum principal stress
P_1	Maximum principal stress

The original Beremin model calculates fracture probabilities based on a representative elementary volume (REV) which contains at least one crack initiation site. The stress value in the REV used for evaluation is taken to be constant. The heterogeneous nature of local stress distribution has been neglected. Recently, crystal plasticity based approaches have been introduced to the probabilistic

$\dot{\underset{\sim}{F}}_p$	Rate of the plastic deformation gradient
$\underset{\sim}{F}$	Deformation gradient tensor
$\underset{\sim}{F}_e$	Elastic part of the deformation gradient tensor
$\underset{\sim}{F}_p$	Plastic part of the deformation gradient tensor
$\underset{\sim}{L}_p$	Plastic velocity gradient tensor
$\underset{\sim}{M}$	Mandel stress tensor
$\underset{\sim}{N}$	Schmid tensor
$\underset{\sim}{S}$	Piola–Kirchhoff stress tensor
$\underline{m}$	Slip direction vector
$\underline{n}$	Normal vector to the slip plane
a^{sj}	Effective interaction coefficients between slip system s and j
a^{sj}_{ref}	Reference interaction coefficients between slip system s and j
a_{carb}	Carbide strengthening coefficient
b	The norm of Burgers vector
d_{grain}	Average grain size
E	Young's modulus
f_{HZ}	Fraction of hard zone
H	Frequency factor
K	Hall–Petch constant
k	Boltzmann constant
k_m	Constant describing the evolution of β_m
K_{obs}	Constant adjusting contribution from obstacles to mean free path
K_{self}	Constant adjusting contribution from self interactions to mean free path
l_c	Minimum length of a screw dislocation segment
l^s_{sc}	Average length of screw dislocation segments
n	Rate sensitivity power
n_c	Carbide density
$P(P_1 < \sigma_1)$	Probability to find P_1 lower than a given value σ_1
$P(\sigma^* > \sigma_c(r))$	Failure probability induced by a carbide
$P(carb)$	Failure probability induced by all carbides
$P(V_0)$	Failure probability of an elementary volume
P_f	Global cleavage failure probability
q_m	Constant describing the evolution of γ_m
r	Carbide size (radius)
T	Temperature
T_0	Master Curve Reference Temperature
υ	Poisson's ratio
y^s	Critical distance for dislocation annihilation
y^s_{drag}	Critical distance for dislocation annihilation in the drag regime (high temperature)

modelling of brittle fracture [13–18]. The constant stress value in the REV used by the original Beremin model is then replaced by a stress distribution function evaluated by crystal plasticity. This approach allows the integration of multiple microstructural factors into the prediction in a physical way, such as crystallographic orientations, grain size effects and irradiation effects [19].

One of the objectives of the current work is to investigate the stress localization in steels with different carbon contents. Another objective is to present a workflow for identifying and applying a dislocation density based crystal plasticity model using the FFT solver AMITEX_FFTP[1] in the prediction of brittle fracture. The paper is structured as follows: a brief introduction of materials used for studying the segregation effect is given in Section 2. Observations of microstructures are also recalled. Results of tensile tests combined with image-based measurement are described in Section 2.3. The crystal plasticity model used for the current study and the parameter calibration process are presented in Section 3. The simulation results of macroscopic fracture toughness are given in Section 4 and compared to experimental data.

[1] https://amitexfftp.github.io/AMITEX/index.html.

Fig. 1. Grain morphology measured by EBSD for each material (300 μm × 225 μm). The colours represent Euler angles.

Table 1
Chemical compositions of the three model alloys (wt%) [20].

Material	C	S	P	Si	Mn	Ni	Cr	Mo	Cu	Al	N
0.38%C	0.376	0.0048	0.008	0.265	1.626	0.891	0.142	0.580	0.002	0.023	0.0085
0.29%C	0.292	0.0029	0.006	0.236	1.512	0.839	0.132	0.540	0.002	0.018	0.0057
0.19%C	0.189	0.0013	0.004	0.188	1.386	0.764	0.122	0.484	<0.001	0.02	0.0026

Table 2
Carbide characteristics and grain size.

Model alloys	Zone	f_{HZ} %	Nb of carbides	Nb of carbides/μm^2	M_2C portion	Grain size D_{eq} (μm)
0.38%C	Hard	22	6207	1.60		3.0
	Soft		3293	0.85		3.9
	Weighted average			1.01	0.11	3.0
0.29%C	Hard	6	5471	1.41		2.9
	Soft		1997	0.51		4.5
	Weighted average			0.57	0.075	3.5
0.19%C	Hard	4	6183	1.59		2.8
	Soft		1736	0.45		4.4
	Weighted average			0.49	0.065	5.4

2. Materials and macroscopic mechanical properties

2.1. Chemical compositions

To investigate the macro-segregation of carbon in large forgings, three synthetic alloys were made by Framatome [20]. The chemical compositions of these three alloys are shown in Table 1. These three materials were named after their carbon content (wt%) in the current work whose values are 0.38%, 0.29% and 0.19% in weight, respectively. Variations of other chemical elements could also be noticed. These characteristic compositions were determined by taking into account co-segregations that occur in the actual macro-segregated zones.

2.2. Microstructures and carbide distributions

Scanning electron micrographs of polished and etched samples were used to quantitatively determine the statistics of carbides as presented in Table 2. Heterogeneous segregation areas of a few hundred micrometres wide have been identified in these materials. The micro-segregated zones show higher indentation hardness which are denoted as hard zones. The carbide number density of each material is a weighted average based on the hard–soft zone ratio. Different types of carbides are found in these materials. About 90% carbides are Fe_3C cementite precipitates which mainly exist in intergranular positions and are of large size. It is thus reasonable to assume that Fe_3C only contributes to the fracture and not to the hardening. The smaller carbides of type M_2C found in intragranular positions are assumed to be the only contributor for precipitation strengthening. The proportion of M_2C in the total population of carbides are estimated thanks to Thermocalc calculation which is added in the table. D_{eq} is the equivalent diameter of grains. More details can also be found in [21]. The average grain sizes are measured by EBSD and calculated with weighted average based on the hard–soft zone ratio.

The EBSD maps of these 3 materials are shown in Fig. 1. It can be noticed that smaller packets and blocks are found in 0.38%C material. This observation is in accordance with the work of Morito et al. [22]. The microstructure might have changed from upper bainite to lower bainite or martensite for higher carbon content.

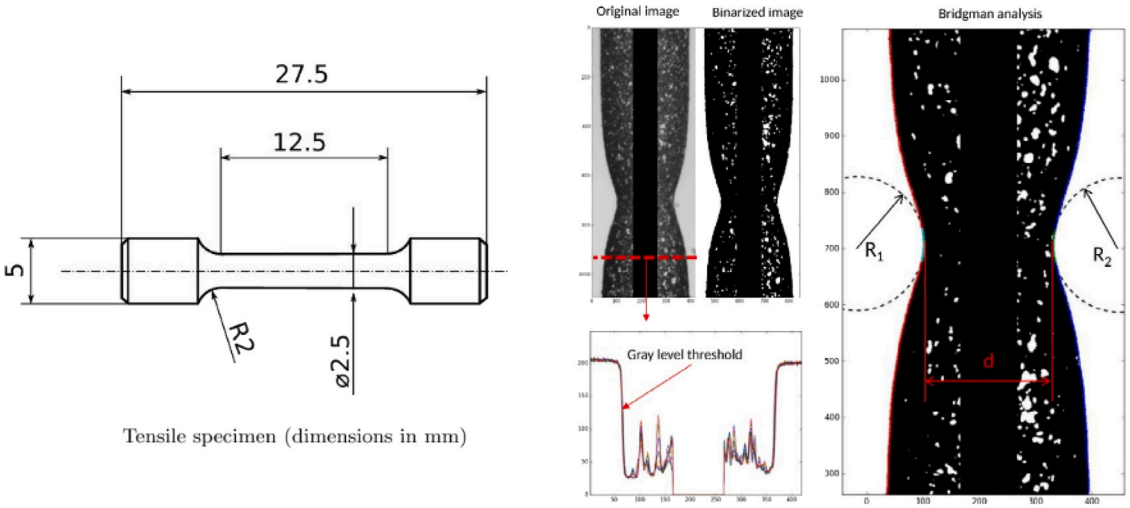

Fig. 2. Tensile specimen and Bridgman correction.

2.3. Mechanical properties determined by tensile tests

Tensile tests were performed at room temperature, the ductile–brittle transition reference temperature T_0 and 2 temperatures around T_0 for each material. This reference temperature was determined by the multi-temperature method given by ASTM E1921 [23]. For 0.19%C material, $T_0 = -123\,°C$ and the testing temperatures are $-110\,°C$, $-130\,°C$, $-150\,°C$ and $20\,°C$. For 0.29%C and 0.38%C materials, $T_0 = -75\,°C$ and the corresponding testing temperatures are $-50\,°C$, $-70\,°C$, $-90\,°C$ and $20\,°C$. The Master curves with fracture toughness data of these 3 materials are reproduced in Appendix. More details about the ductile to brittle transition temperature and fracture toughness tests can also be found in [21]. All of the tensile tests were conducted at strain rate $10^{-4}\,s^{-1}$.

Axisymmetric smooth tensile specimens have been used to perform tensile tests whose geometry is shown in Fig. 2. All of these tensile specimens were extracted from the halves of tested Charpy specimens. These Charpy specimens have a reduced thickness of 5 mm instead of 10 mm. Their exact dimensions are as follows: 5×10×55 mm. The conventional experimental setup using a longitudinal clip-on extensometer was used to obtain the true stress–strain relationship up to the onset of necking. In order to obtain the true stress–strain information afterwards, the cross-section reduction was also measured for the post-necking part with image-based approaches as shown in Fig. 2. With the onset of necking, non-uniform deformation begins. The stress state in the cross-section turns out to be a non-uniform triaxial stress field. Thus, the Bridgman correction was applied to compute the stress in the minimum cross-section of the specimen.

The true stress–strain curves for the three materials are plotted in Fig. 3a–c. The evolution of the yield strength as a function of temperature is presented in (d). Highest yield strength can be observed for the material with 0.38%C.

2.4. Determination of triaxiality loading condition

Fracture toughness tests are usually conducted with pre-cracked compact tension (CT) specimens. Performing crystal plasticity simulations under the stress triaxiality level at crack fronts of CT specimens is of great interest to reproduce the actual local stress states. The stress triaxiality is defined by $\eta = \frac{\sigma_m}{\sigma_{eq}}$, where σ_m is the hydrostatic stress and σ_{eq} is the Von Mises equivalent stress. η was measured through post-processing with CT simulations. Using the numerical results presented in [21], the stress field in each element produced by finite element calculations can be obtained. The evolution of triaxiality was calculated in the element that has the greatest maximum principal stress (P1). The element with the greatest P1 stress does not always remain in the first layer of elements to the crack tip. The difference is shown in Fig. 4b–d. So it will be more suitable to calculate the triaxiality by tracking the element presenting the greatest P1 stress as the fracture is assumed to depend on it. The range of experimentally measured crack mouth opening distance (CMOD) at fracture collected from all the specimens under the same testing condition is marked with dashed lines in Fig. 4b–d. The average triaxiality value is then calculated using data within this interval. An average triaxiality is obtained for each material following this procedure. For simplicity, an approximated value $\eta = 2.15$ is taken as the triaxiality condition in the following crystal plasticity calculations for the three materials. In addition, the largest P1 stress detected in elements within the fracture CMOD interval is around 2240–2490 MPa for 0.38%C, 1870–2170 MPa for 0.29%C and 1790–2200 MPa for 0.19%C.

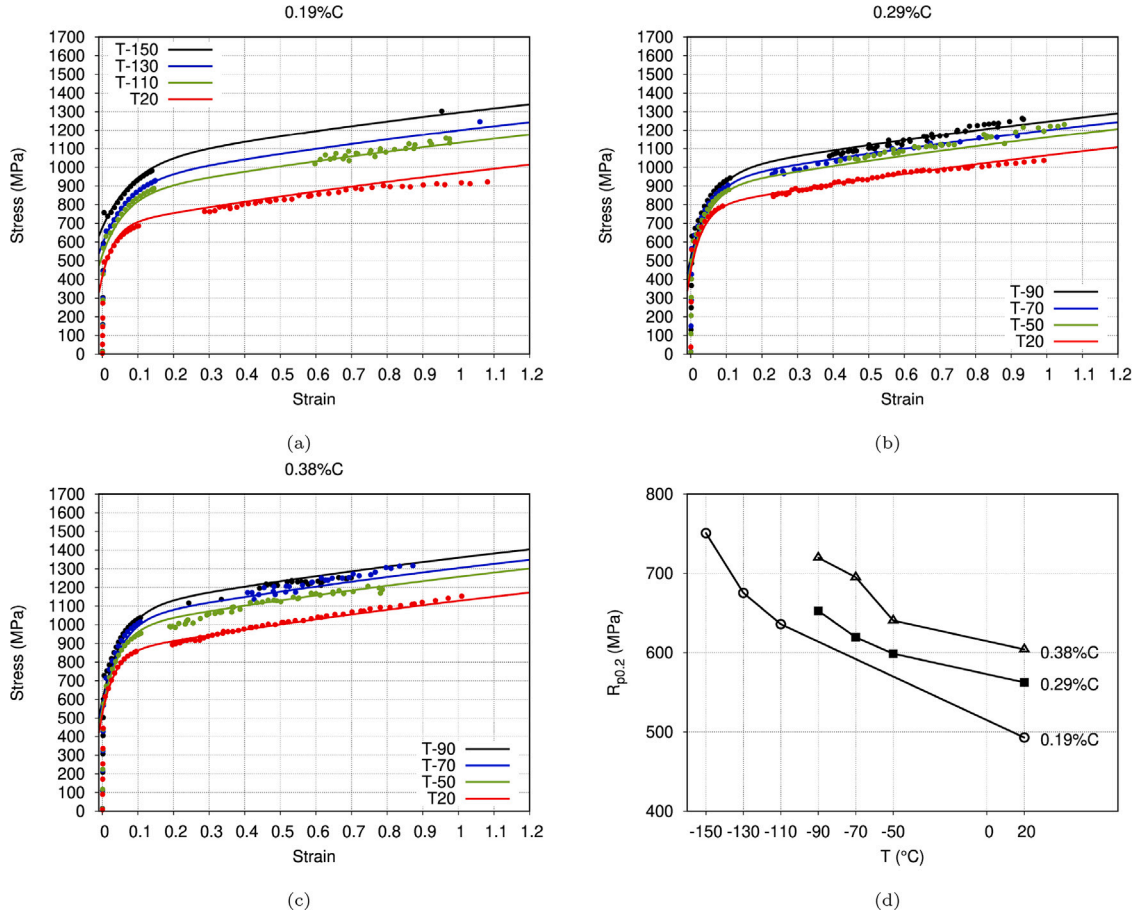

Fig. 3. (a)(b)(c) Stress–strain curves with Bridgman correction (dots) and identified elasto-plastic law (line) (see [21]). (d) yield strength evolution.

3. Crystal plasticity model and identification

3.1. Constitutive equations

A simplified version without the irradiation effect of Monnet's model [19] is used for the current study. The constitutive laws took into account dislocation density evolution, grain size effect (Hall–Petch) and carbide precipitates. Particular attention has been paid to the role of carbide hardening. For BCC structure, slip is expected to occur on the 24 slip systems $\{110\}\langle 111\rangle$ and $\{112\}\langle 111\rangle$.

This crystal plasticity model also introduced a smooth transition between the thermally activated regime (below 250 K) and the athermal regime (above 350 K) by a harmonic superposition. At higher temperatures, the dislocation mobility is governed by jog-drag, while lattice friction is dominant in the thermally activated regime. The total contribution to slip rate is written as:

$$\frac{1}{\dot{\gamma}^s} = \frac{1}{\dot{\gamma}^s_{drag}} + \frac{1}{\dot{\gamma}^s_{friction}} \tag{1}$$

where the upper index 's' refers to the slip system number.

The jog-drag driven rate evolution is given by:

$$\dot{\gamma}^s_{drag} = \dot{\gamma}_0 \left(\frac{|\tau^s|}{\tau^s_c} \right)^n \operatorname{sign}(\tau^s) \tag{2}$$

where constant $\dot{\gamma}_0 = 10^{-5}\,\mathrm{s}^{-1}$. τ^s is the resolved shear stress on the system s. The critical resolved shear stresses for slip τ_c is expressed later in Eq. (7).

The shear rate induced by lattice friction is given by:

$$\dot{\gamma}^s_{friction} = \rho^s_m b H l^s_{sc} \exp\left(-\frac{\Delta G_0}{kT} \left(1 - \sqrt{\frac{\tau^s_{eff}}{\tau^s_0}} \right) \right) \operatorname{sign}(\tau^s) \tag{3}$$

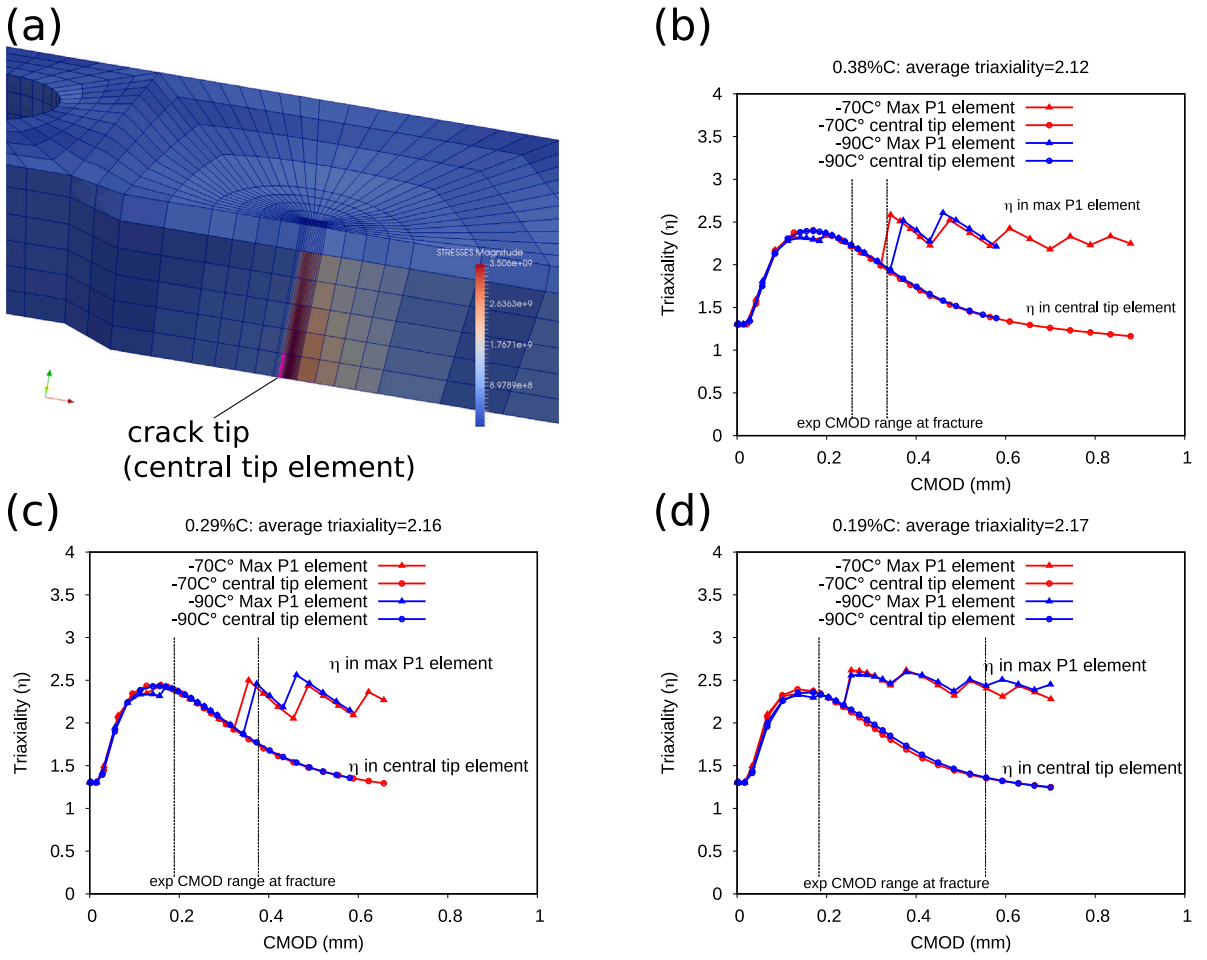

Fig. 4. Determination of the stress triaxiality at crack fronts of CT12.5 specimens.

where ρ_m is the mobile dislocation density whose value is taken to be constant and equal to the initial dislocation density. b is the norm of the Burgers vector. H is a frequency factor and takes the value of $2\times10^{11}\,s^{-1}$. ΔG_0 is the reference slip activation energy which takes 0.84 eV. The critical shear stress τ_0 for {110} planes is 360 MPa. Different values of τ_0 are taken for {112} planes in the twinning (TW) direction (410 MPa) and in the anti twinning (AT) direction (480 MPa). These parameters are adjusted according to previous experimental results [19]. l_{sc} represents the average length of screw dislocation segments which is expressed by the following Eq. (4).

$$l_{sc}^{s}=\max\left[\lambda^{s}-\alpha^{s}\frac{\mu b}{\tau_{eff}^{s}};l_{c}\right],\quad \frac{1}{\lambda^{s}}=\min\left[\sqrt{\rho_{obs}^{s}};\frac{\mu b}{\tau_{eff}^{s}}\rho_{obs}^{s}\right] \tag{4}$$

where λ^s is the average obstacle spacing. l_c is the minimum length of a screw dislocation segment. μ is the shear modulus. α^s represents the strengthening effect of obstacles on system s, which is expressed in Eq. (11). ρ_{obs} is the density of total local obstacles that are dislocations and carbide precipitates in the current work:

$$\rho_{obs}^{s}=\sum_{j\neq s}\rho_{dis}^{j}+\rho_{carb} \tag{5}$$

τ_{eff} is the effective stress to activate dislocation motion:

$$\tau_{eff}^{s}=\max\left\{0;|\tau^{s}|-\tau_{c}^{s}\right\} \tag{6}$$

The critical stress τ_c accounts for the contribution from the self-interaction of dislocations in the same slip system (τ_{self}), the Hall–Petch effect (τ_{HP}), and the line tension contribution (τ_{LT}),.

$$\tau_{c}^{s}=\sqrt{{\tau_{self}^{s}}^{2}+{\tau_{LT}^{s}}^{2}}+\tau_{HP}^{s} \tag{7}$$

The self-interaction term is given by:

$$\tau^s_{self} = \mu b\sqrt{a^{ss}\rho^s_{dis}} \tag{8}$$

where a^{ss} is the interaction coefficient as shown in Eq. (12). For self-interaction, only the interactions on the same slip system is considered. ρ^s_{dis} is the updated dislocation density on the slip system s. μ is the shear modulus, b is the norm of the Burgers vector. The HP term reads:

$$\tau^s_{HP} = \frac{\mu}{\mu_{300K}}\frac{K}{\sqrt{d_{grain}}} \tag{9}$$

where the HP constant $K = 0.17$ for RPV steel [19]. d_{grain} denotes the grain size. μ_{300K} is the shear modulus at 300 K.

The line tension term is given by:

$$\tau^s_{LT} = \max\left[\frac{\alpha^s \mu b}{\lambda^s - l_c} - \tau^s_{eff}, 0\right] \tag{10}$$

As mentioned before, the obstacle strength in system s is

$$\alpha^s = \frac{1}{\sqrt{\rho^s_{obs}}}\sqrt{\sum_{j\neq s} a^{sj}\rho^j_{dis} + a_{carb}\rho_{carb}} \tag{11}$$

where the interaction coefficient is given by:

$$a^{sj} = \left(0.2 + 0.8\frac{\ln(0.35b\sqrt{\rho_{obs}})}{\ln(0.35b\sqrt{\rho_{ref}})}\right)^2 a^{sj}_{ref} \tag{12}$$

where $\rho_{ref} = 10^{12}\,\mathrm{m}^{-2}$. The interaction matrix a^{sj}_{ref} only depends on 5 parameters. The interaction matrix presented by Monnet et al. [19] is adopted here.

The evolution of defect densities is formulated with the Kocks–Mecking equation:

$$\dot{\rho}^s_{dis} = \frac{|\dot{\gamma}^s|}{b}\left[\frac{1}{\Lambda^s} - y^s\rho^s_{dis}\right] \tag{13}$$

$$\frac{1}{\Lambda^s} = \frac{1}{d_{grain}} + \left(1 - \frac{\tau^s_{eff}}{\tau_0}\right)\left(\frac{\sqrt{\alpha^{ss}\rho^s_{dis}}}{K_{self}} + \frac{\alpha^s\lambda^s\rho^s_{obs}}{K_{obs}}\right) \tag{14}$$

$$\frac{1}{y^s} = \frac{1}{y^s_{drag}} + \frac{2\pi\tau^s_{eff}}{\mu b} \tag{15}$$

where K_{self} and K_{obs} are constants to be adjusted.

The current crystal plasticity model is implemented within the finite strain framework. The deformation gradient can be decomposed into two parts: elastic and plastic parts:

$$\underset{\sim}{\boldsymbol{F}} = \underset{\sim}{\boldsymbol{F}}_e\underset{\sim}{\boldsymbol{F}}_p \tag{16}$$

The Mandel stress $\underset{\sim}{\boldsymbol{M}}$ and the second Piola–Kirchhoff stress $\underset{\sim}{\boldsymbol{S}}$ were shown to be work-conjugate to provide accurate stress measure in crystal plasticity [24,25]. According to the approach of Mandel, the resolved shear stress τ^s projected in each slip system can be computed as:

$$\tau^s = \underset{\sim}{\boldsymbol{M}} : \underset{\sim}{\boldsymbol{N}}^s = (\underset{\sim}{\boldsymbol{F}}^T_e\underset{\sim}{\boldsymbol{F}}_e\underset{\sim}{\boldsymbol{S}}) : \underset{\sim}{\boldsymbol{N}}^s \tag{17}$$

with the Schmid tensor $\underset{\sim}{\boldsymbol{N}}^s = \underline{\boldsymbol{m}}^s \otimes \underline{\boldsymbol{n}}^s$. $\underline{\boldsymbol{m}}^s$ is the slip direction vector and $\underline{\boldsymbol{n}}^s$ is the normal vector to the slip plane of system s.

The evolution equation for the plastic deformation gradient can be expressed as [26]:

$$\dot{\underset{\sim}{\boldsymbol{F}}}_p = \underset{\sim}{\boldsymbol{L}}_p\underset{\sim}{\boldsymbol{F}}_p \tag{18}$$

The plastic velocity gradient tensor $\underset{\sim}{\boldsymbol{L}}_p$ is the sum of the slip rates in all slip systems:

$$\underset{\sim}{\boldsymbol{L}}_p = \sum_{s\in slip}\dot{\gamma}^s\underline{\boldsymbol{m}}^s \otimes \underline{\boldsymbol{n}}^s \tag{19}$$

3.2. Determination of parameters related to hardening

The geometry used for this rapid parameter optimization is constituted by 9 × 9 × 9 equal-sized cubic voxels. 729 randomly generated crystal orientations are attributed to this geometry. Each voxel represents an orientation as shown by different colours in Fig. 5a. Experimental tensile curves at different temperatures are used for this inverse identification process.

Alloys used in the current study are similar to the RPV steel described in [19] to some extent. The identification has been simplified by taking some parameters from the literature as presented in Table 3. Parameters identified by this inverse calibration

Table 3
Values of parameters obtained from literature.

Variable	Value
$\dot{\gamma}_0$ (s^{-1})	2×10^{-5}
ΔG_0 (eV)	0.84 eV
H (s^{-1})	2×10^{11}
E (Young modulus) (GPa)	205–0.0459 T
υ (Poisson's ratio) (GPa)	0.3
$\tau_0\{110\}$ (MPa)	360
$\tau_0\{112\}TW$ (MPa)	410
$\tau_0\{112\}AT$ (MPa)	480
b (Burgers vector nm)	0.248
K_{forest}	$K_{self}/3$
n	100
a_{ref}^{xj} (collinear interaction)	0.7
a_{ref}^{xj} (other)	0.1
a_{carb}	1.0

Table 4
Identified parameters and material constants used for this crystal plasticity model.

Material/Variable	d_{grain} (μm)	K_{self}	y_{drag} (nm)	ρ_{carb} (mm^{-2})	ρ_{ini} (mm^{-2})	l_c (nm)
0.38%C	3.7	5.7–7.4	6	6.977×10^6	3.3×10^7	2
0.29%C	4.4	7.0–7.8	6	6.409×10^6	2.7×10^7	2
0.19%C	6.9	8.2	6	6.240×10^6	1.4×10^7	2

approach are shown in Table 4. As mentioned in the previous section, only M_2C precipitates are supposed to participate in the hardening. Carbide density ρ_{carb} is derived based on experimental measurements of M_2C as shown in Table 2. These values are fixed during the optimization. Measured grain size values d_{grain} are introduced in the optimization process as initial values. It can be noticed that for 0.38%C and 0.29%C the final values of d_{grain} are very close to measured ones. For 0.19%C, better results were achieved with a relatively larger grain size value. K_{self} is identified to be slightly temperature-dependent. The annihilation distance y_{drag} remains the same for these 3 materials. ρ_{ini} is identified to increase with carbon content. The minimum length of screw segments is taken equal to 2 nm for all three materials. The final results are shown in Fig. 5b–d.

3.3. Validation of calibrated model at constant triaxiality $\eta = 1/3$

Validation tests were firstly conducted under constant triaxiality conditions with $\eta = 1/3$. In tensile tests, stress triaxiality is 1/3 up to necking so that simulation results could be compared directly with tensile curves. As shown in Fig. 6a, a REV containing 729 grains are generated with the help of Neper [27]. This geometry is then discretized with 100 × 100 × 100 cubic voxels. 729 randomly generated crystalline orientations are applied to these grains. The parameters calibrated for 0.38% material at −50 °C and −70 °C are used for these validation tests. The real microstructure is not taken into account in these tests. The average stresses at different strain levels are computed based on all voxels. The experimental curves are compared with the average stress curves in Fig. 6b which shows good agreement.

4. Crystal plasticity simulations based on EBSD

Compared with conventional Finite Element Methods, FFT based method could significantly reduce the computation time thanks to its better parallel computing capability. FFT methods intrinsically use image-type 3D grids thus can be adapted to image-based modelling conveniently [28]. The microstructural unit-cells (or REV) are regularly discretized in a 3D image of voxels. In the current section, all the microstructural unit-cells are extracted from EBSD data with single layer voxels. We will at first specify the methods we used and discuss the stress distributions observed in these 3 materials with different carbon contents.

4.1. Stress average method

The MIBF model takes into account the stress heterogeneities within the REV [17]. For bainitic steels, the REV contains many bainitic packets. Carbides are embedded in these packets and act as crack initiators. The stress is assumed to be homogeneous within each packet and act as a driving force for crack initiation. According to this consideration, the stress needs to be averaged in each packet at first instead of collecting directly from each voxel (voxel method). The obtained averaged stress is then attributed to each voxel in the same packet (grain average method). The total number of data points remains the same in each packet so that the size of grains can be taken into account through this weighting method. A difference could be observed for these two methods as shown in Fig. 7a. As expected, it can be noticed that this averaging method eliminates the extreme values and gives a more concentrated distribution. The maximum principal stress P_1 field obtained by this grain average method is compared with the original simulation results in Fig. 7b.

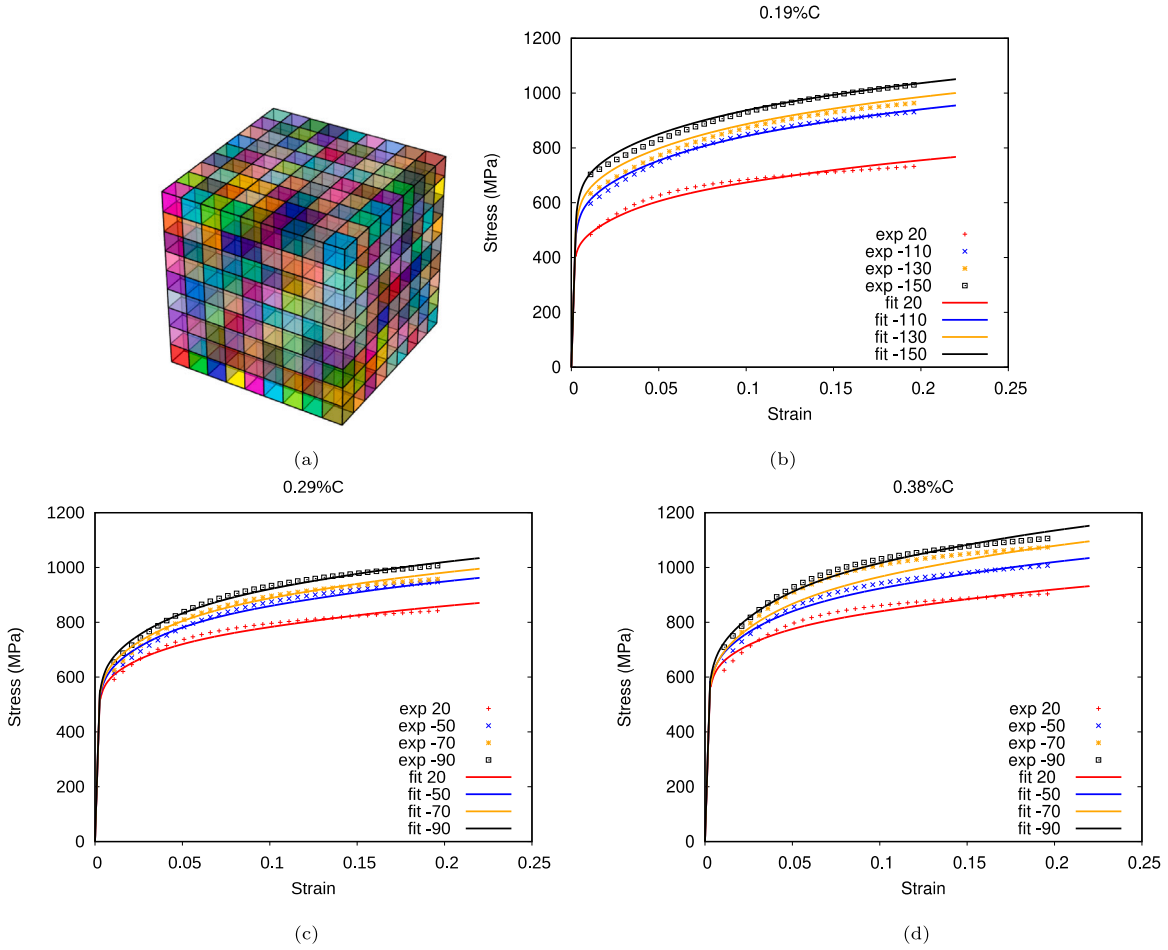

Fig. 5. (a) Geometry used for parameter optimization in AMITEX_FFTP (729 material orientations, 1 cubic voxel per orientation), and comparison with experimental tensile curves for each material (b)(c)(d).

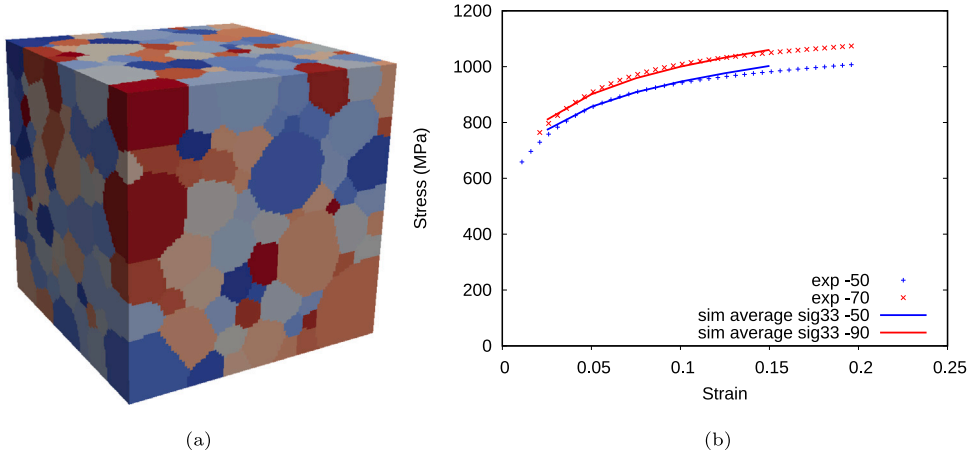

Fig. 6. Validation tests with constant triaxiality (η=0.33) loading.

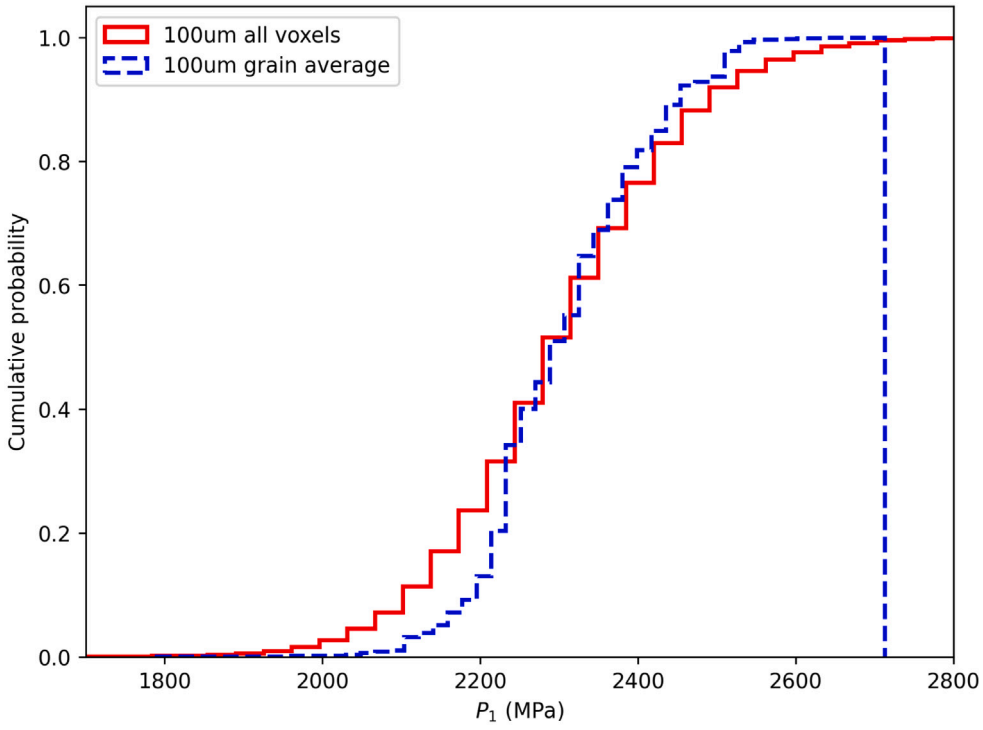

(a)

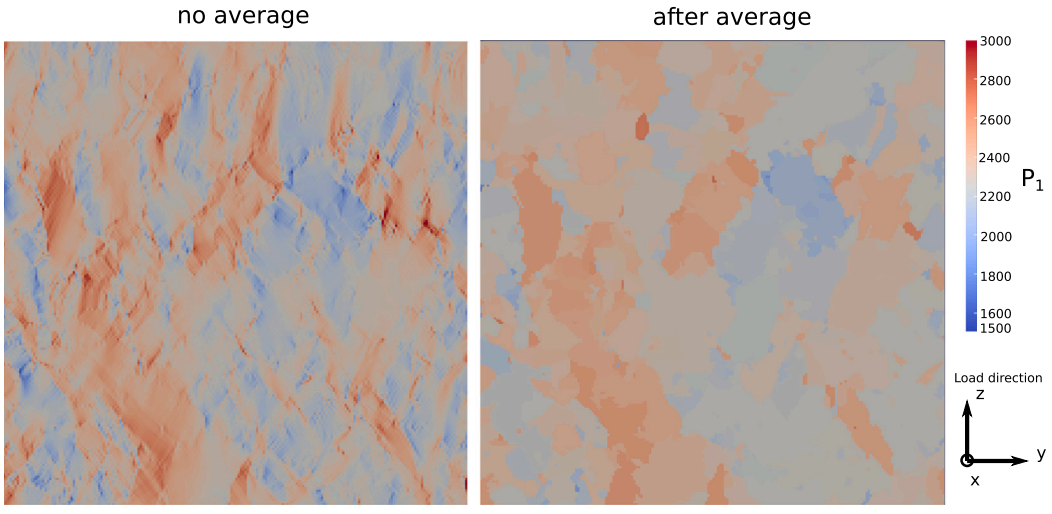

(b)

Fig. 7. Principal stress field before and after averaging within each packet.

4.2. Sampling size effect

The size of the selected area on the EBSD map may have an impact on the final stress statistics. Voxel-based REVs are selected from the EBSD map of the 0.19%C and 0.29%C materials as shown in Fig. 8. The REV of the 30×30 μm region of the 0.19%C material contains 55 grains with different crystallographic orientations and was discretized with 150 × 150 voxels. The 100×100 μm REV of the 0.19%C material contains 589 orientations and are discretized with 200 × 200 voxels. The principle stress values were analysed using the grain average method as presented in the previous section. The REVs of the 0.29%C material are voxelized with the same number of voxels as those of 0.19%C. The 30×30 μm and the 100×100 μm REV contain 77 and 403 orientations respectively. We

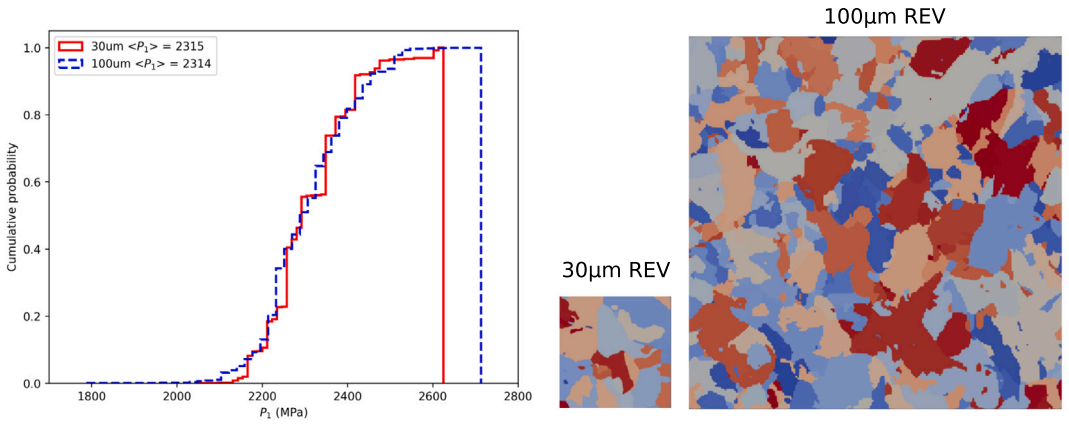

(a) 0.19%C

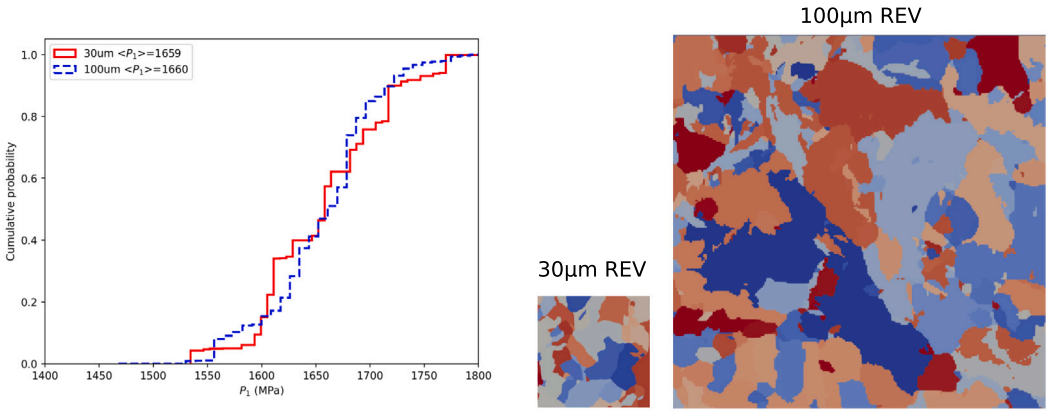

(b) 0.29%C

Fig. 8. Stress distribution obtained for different sampling sizes.

name $\langle P_1 \rangle$ the average maximum principal stress. For the same $\langle P_1 \rangle$, the cumulative distribution curves obtained from these two REVs are very close as shown in Fig. 8. No significant REV size effect has been observed although the stress distribution expands to a larger range for the larger REV. We thus assume that the REV size effect is very limited for these materials from 30 μm to 100 μm sampling range. It is considered acceptable to use stress distributions obtained with different REV sizes. However, we kept the standard 50 μm element size in front of the crack tip of a CT specimen in the macroscopic simulations to have sufficient mechanical fields and avoid quasi-singularities.

4.3. Effect of refined microstructures on stress distribution

For the 0.38%C material, the EBSD map reveals two distinct zones as shown in Fig. 9. The hard zone (hz) corresponds to the micro-segregated zone which shows lath structure. The hardness in these zones is much higher than that found in the soft zone. The hard zone could be easily identified from its darker colour in the grain boundary map in Fig. 9. The soft zone (sz) is the non-segregated zone whose microstructure is like the other materials with lower carbon contents (0.19%C and 0.29%C). The REVs for FFT simulations are firstly selected from two zones of 30 × 30 μm as indicated in Fig. 9. The soft zone and hard zone contain 101 and 379 orientations respectively. Simulations of these different zones are all conducted with material parameters of 0.38%C as presented in Tables 3 and 4.

Fig. 10 shows the P_1 stress map obtained from these 30 × 30 μm REVs at $\langle P_1 \rangle \approx 2000$ MPa. The voxelized REVs could be found in Figs. 8 and 9. It can be noticed that the maximal P_1 stress is located close to some grain boundaries. For the hard zone of 0.38%C material, it is more frequent to find high stress concentration on refined grains and grain boundaries.

Fig. 11 presents the P_1 stress distributions obtained in the hard zone and soft zone. The effect of microstructures can be observed. At the same average strain level (4% and 2.5% for example), the stress distribution showed significant differences. The stress

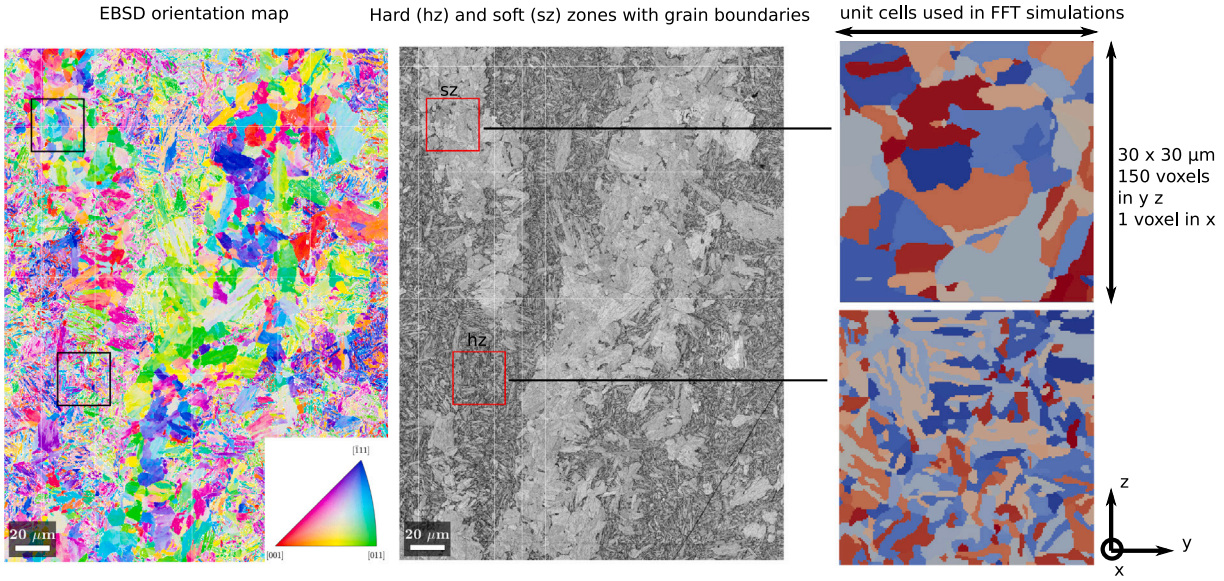

Fig. 9. REVs used for FFT simulations constructed from EBSD data of 0.38%C material.

distribution shifts towards a higher value and distributes in a larger range in the hard zone. In the soft zone, the stress distribution is less heterogeneous and more concentrate on a smaller value.

The effect of microstructure is less significant when comparing the stress distributions at the same $\langle P_1 \rangle$ level as shown in Fig. 12. It can be noticed that the stress distribution in the hard zone is slightly less concentrated compared with that in the soft zone of 0.38%.

As shown in Table 2, the hard zone accounts for 22% of the area in the 0.38%C material. Another zone was selected from the EBSD data respecting the hard zone to soft zone ratio as shown in Fig. 13. The right lower part is the hard zone with smaller grains. The boundary between the soft and hard zone is marked with a dashed green line in Fig. 13. Simulations were conducted with parameters from 0.38%C material. It is more frequent to find the stress localization spots in the hard zone. The stress distribution at the same $\langle P_1 \rangle$ level obtained from this hybrid microstructure is shown in Fig. 12. The distribution is not exactly in between the pure hard zone and soft zone curves, although they are very close. This might be a sign of a "mesoscopic" incompatibility between the hard zones and soft zones. The stress distributions of 0.29%C and 0.19%C materials at the same $\langle P_1 \rangle$ level are also shown in Fig. 13. It is however worth noting that the stress distribution of 0.38%C material is more homogeneous compared with the other 2 materials with less carbon content. Simulations have also been conducted using the same set of material parameters for all of three microstructures. The change of constitutive parameters does not affect the stress distribution at the same $\langle P_1 \rangle$ level. We therefore believe that the difference is caused by the microstructural evolution observed in 0.38%C.

4.4. Stress distributions and parameter fitting

The stress distributions have been analysed for each REV and fitted with the 3 parameter Weibull distributions. For the 3 parameter Weibull distribution, the probability for the local maximum principal stress P_1 to be lower than a given value σ_1 is:

$$P(P_1 < \sigma_1) = 1 - \exp\left(-\left(\frac{\sigma_1 - \gamma_m}{\beta_m}\right)^{\alpha_m}\right) \tag{20}$$

Fig. 14 gives an example of the P_1 stress distribution with increasing average principal stress $\langle P_1 \rangle$. It can be noticed that the heterogeneties increase with increasing $\langle P_1 \rangle$ which is consistent with the observation of Libert et al. [14]. Fig. 14b shows the fitting results at each stress level. The 3-parameter Weibull distribution could give good fitting results for the extreme values of the maximum principal stress.

In order to introduce the stress distributions into the MIBF model, a function of $\langle P1 \rangle$ is approximated for each of the 3 parameters of Weibull distribution. The shape parameter α_m is kept constant for all the 3 materials. The difference of these 3 materials is shown by the evolution of the scale parameter β_m and γ_m with $\beta_m = k_m \langle P_1 \rangle$ and $\gamma_m = q_m \langle P_1 \rangle$ (see Fig. 15). There approximated functions were then introduced into the MIBF model in the next section.

Fig. 16 shows the comparison results of the newly obtained stress distributions at a given $\langle P_1 \rangle$ =2200 MPa with that presented by Vincent et al. [13], which was applied in previous studies [17,21]. It can be noticed that less heterogeneity is produced with the current simulations. Compared with the other 2 materials with lower carbon content, the fitted Weibull distribution of 0.38%C case gives less heterogeneity. This result is in agreement with that shown in Fig. 12.

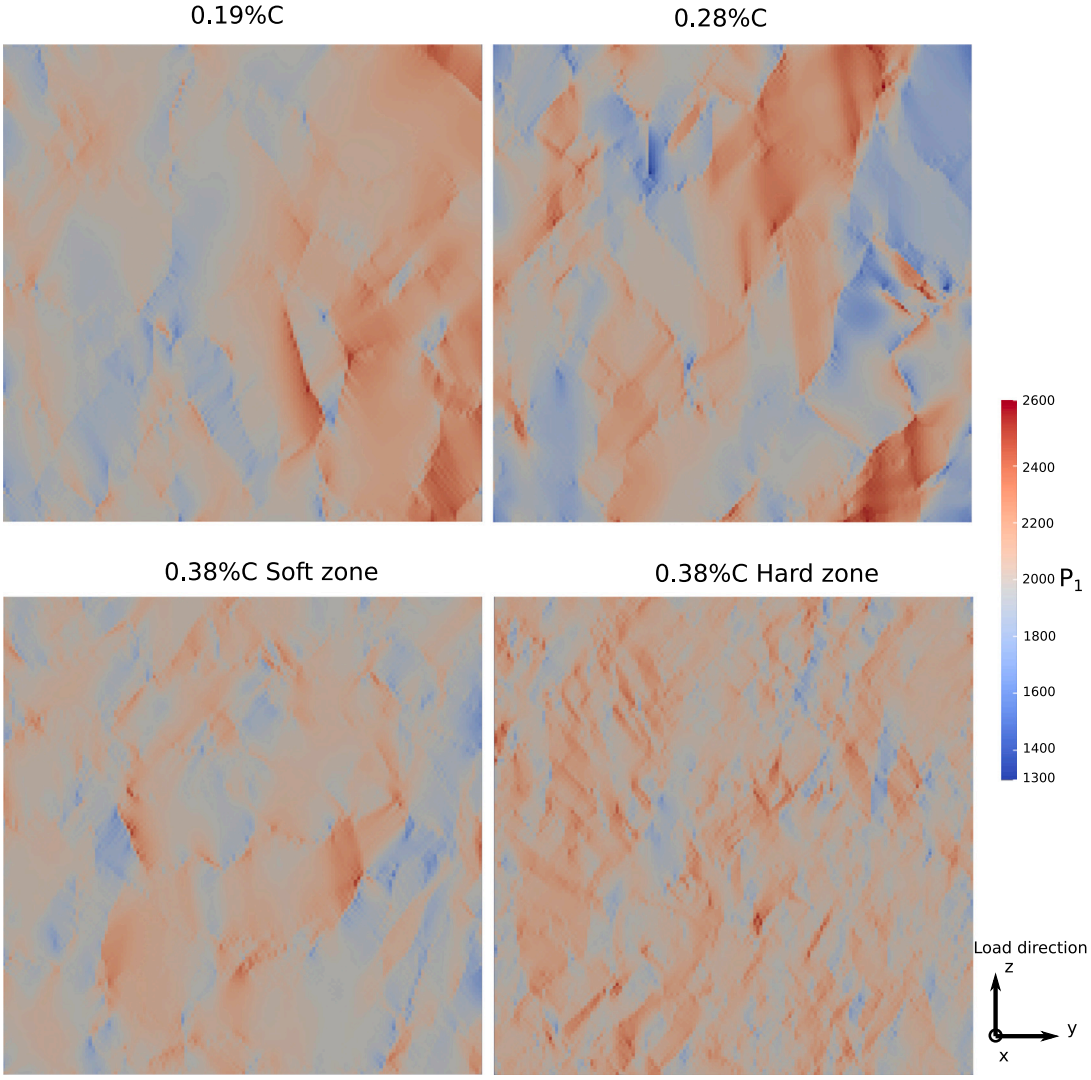

Fig. 10. Maximum principal stress fields (P_1) in 30 ×30 μm REVs of these materials.

Table 5
Parameters of the MIBF model using the 3–parameter Weibull function for maximum principal stress and carbide size distributions.

	γ_f (J m^{-2})	α_m	k_m	q_m	n_c (m^{-3})	α_{carb}	β_{carb} (m)	γ_{carb} (m)
0.19%C	**7.8**	3.0	0.15	0.86	0.34×10^{18}	1.11	0.88×10^{-7}	1.15×10^{-7}
0.29%C	**8.0**	3.0	0.15	0.86	0.43×10^{18}	1.22	1.04×10^{-7}	1.08×10^{-7}
0.38%C	**9.5**	3.0	0.12	0.89	1.02×10^{18}	1.31	1.21×10^{-7}	1.12×10^{-7}

5. Fracture toughness prediction results and discussion

The MIBF model is formulated at different scales from material microstructure to engineering structure level by applying twice the weakest link theory. Studies have shown that, in bainitic steels, firstly microcrack initiates on the cracked particle and across the particle/matrix interface to form a packet size microcrack under the driving force. Microcrack then propagates across a bainite packet boundary leading to the final fracture [29]. In the current MIBF model, the cracking of particles happens once plasticity arises in the surrounding matrix. No other propagation barrier is considered in the current work. The propagation of a crack initiated on a carbide will necessarily lead to the final fracture of the whole structure.

Each carbide embedded in bainitic packets is considered spherical and produces a penny-shaped crack when plasticity arises in the surrounding matrix. The maximum principal stress is considered to be the driving force for the propagation of cracks initiated on

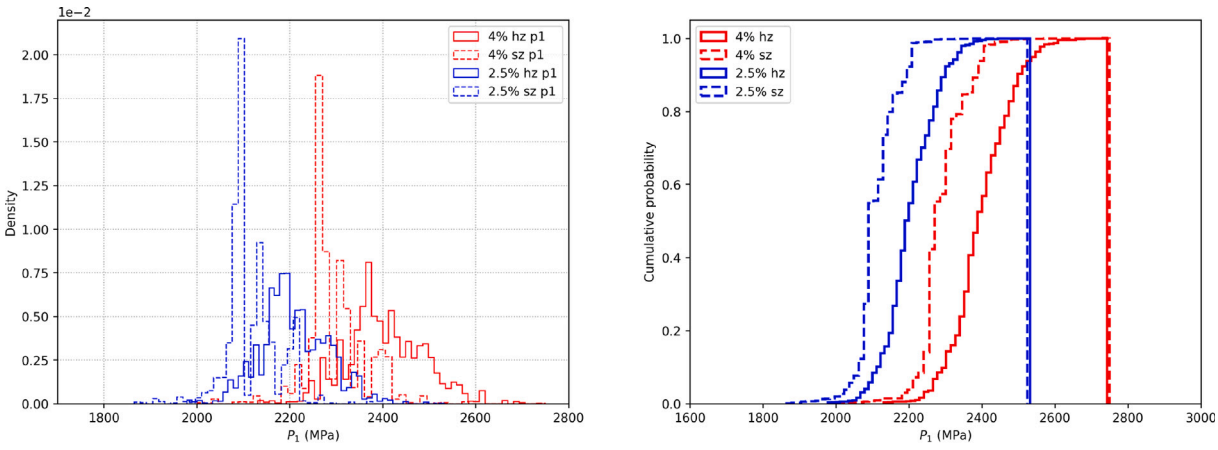

Fig. 11. Principal stress distributions obtained from the hard zone (hz) and soft zone (sz) of 0.38%C material at the same average strain.

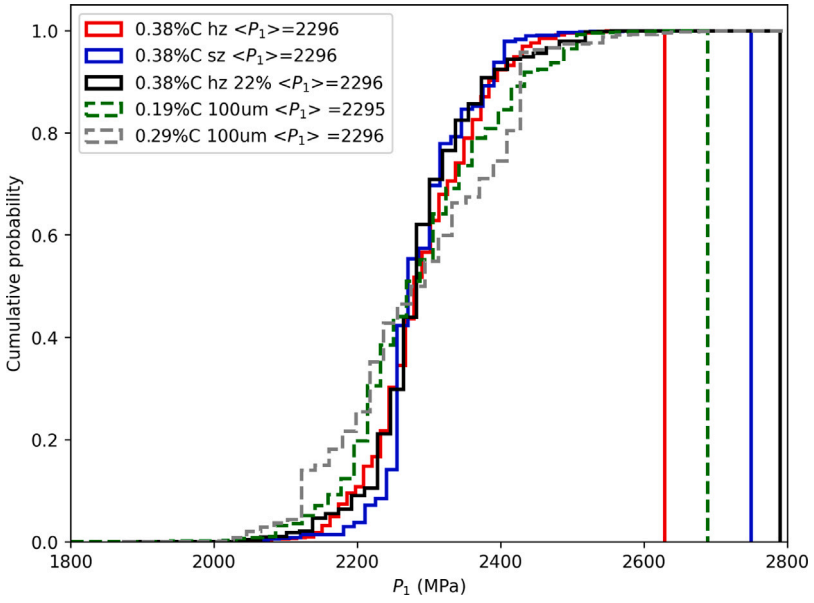

Fig. 12. Soft zone Vs hard zone with the same average maximum principal stress $\langle P_1 \rangle$.

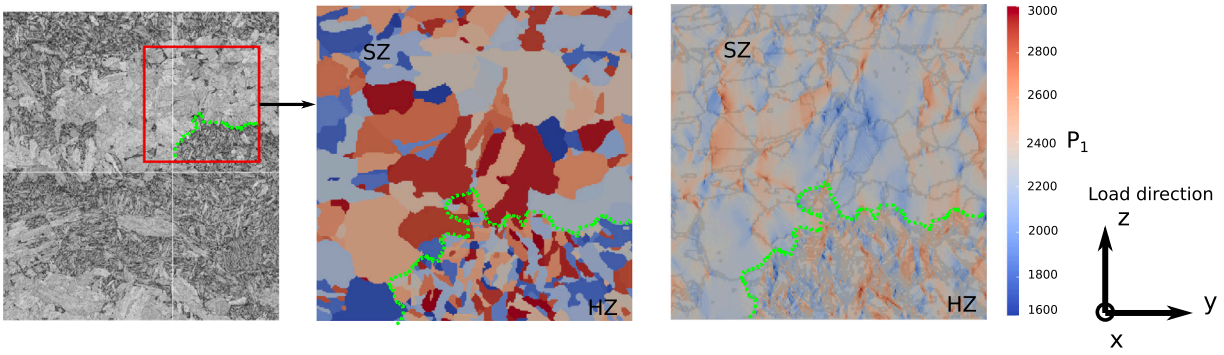

Fig. 13. Region with 22% hard zone: grain structures, 50 ×50 μm voxelized REV and P_1 stress field.

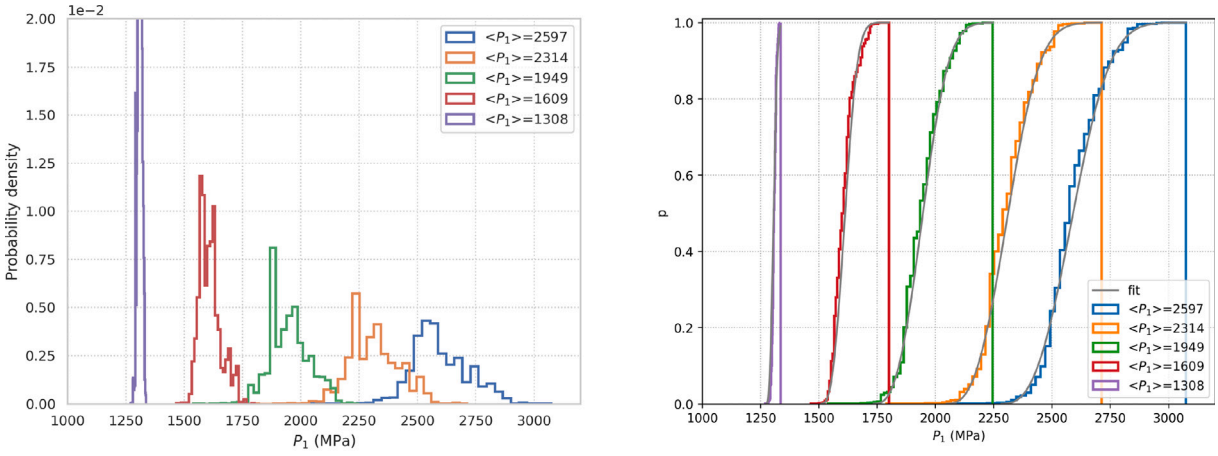

Fig. 14. Principal maximum stresses distributions for increasing average principal stress (0.19%C 100 μm).

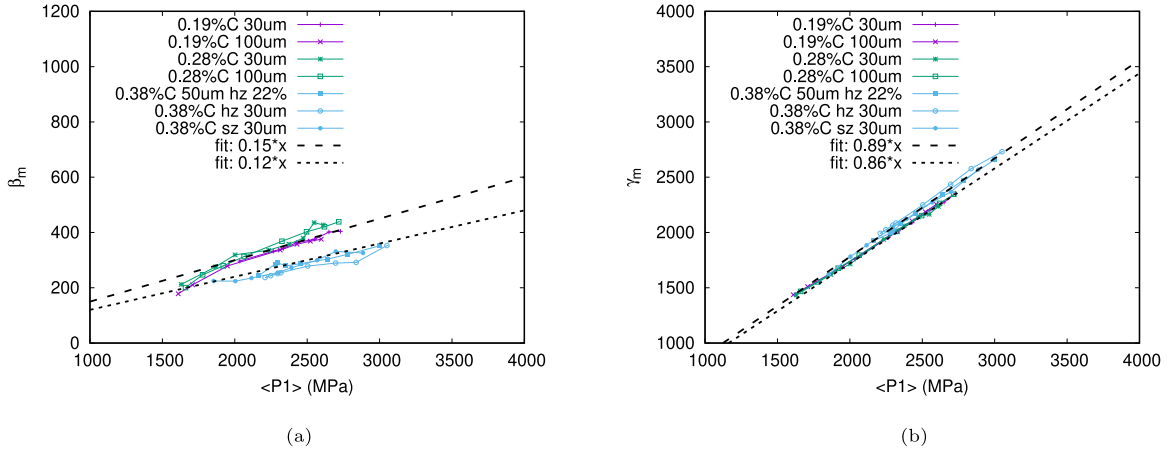

Fig. 15. Evolution of the 3 parameters of Weibull distribution with the average maximum principal stress $\langle P_1 \rangle$.

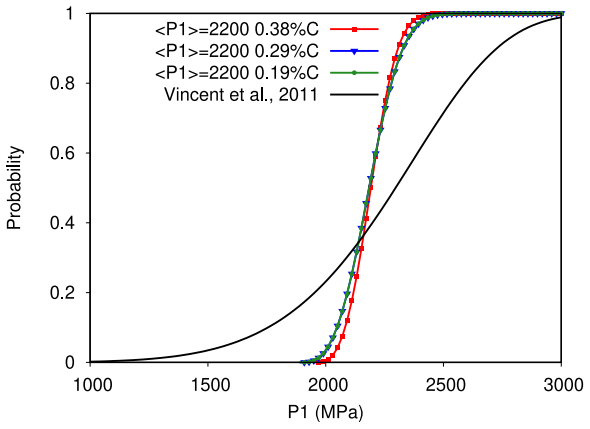

Fig. 16. Stress distributions obtained in the current work compared with previous predictions at a given $\langle P_1 \rangle$.

carbides. Propagation occurs when the driving force reaches the critical fracture stress σ_c, which is given by the Griffith approach:

$$\sigma_c = \sqrt{\frac{\pi E \gamma_f}{2(1-\upsilon^2)r}} \tag{21}$$

where r is the radius of the micro-crack initiated on a carbide, γ_f is the effective surface energy of the material, E is the Young modulus and υ is Poisson's ratio. Numerical evaluation with the MIBF model is based on the elementary volumes V_0 which contains several bainitic packets. Only these V_0 with plastic deformation, which is a sufficient condition for carbide cracking, are taken into account for fracture evaluation. Each V_0 is subjected to a stress field σ_{V_0} under an applied load on the specimen. Due to the crystallographic disorientations, a heterogeneous local stress field is found inside V_0 whose distribution is obtained by previous crystal plasticity simulations. In the current model, the stress field σ^* in a bainitic packet is assumed to be constant.

Therefore, the failure probability induced by a carbide with size r in V_0 is deduced from Eq. (20):

$$P(\sigma^* > \sigma_c(r)) = \exp\left(-\left(\frac{\sigma_c(r) - q_m \left\langle \sigma_{V_0 I} \right\rangle}{k_m \left\langle \sigma_{V_0 I} \right\rangle}\right)^{\alpha_m}\right) \tag{22}$$

where k_m, q_m and α_m are fitted parameters of local stress distributions in V_0 (see Table 5). We also need to consider the influence of carbide size distribution on the failure probability. Thus the carbide size distribution density $dF(r)/dr$ is introduced here as a weight function. The failure probability induced by all carbides with different sizes is expressed by integrating over r:

$$P(carb) = \int_0^{+\infty} \frac{dF(r)}{dr} P(\sigma^* > \sigma_c(r)) dr \tag{23}$$

As presented in Eq. (23), both stress distributions and carbide size distributions contribute to the failure probability and eventually the scattering of fracture toughness. The highest failure probability is reached when both carbide size and stress amplitude are sufficient.

The failure probability of an elementary volume V_0 is obtained by applying the weakest link theory. In other words, the survival probability is the product of all survival events, thus we have:

$$P(V_0) = 1 - (1 - P(carb))^{n_c V_{V_0}} \tag{24}$$

where n_c is the carbide density per volume unit and V_{V_0} is the volume of V_0. At the specimen scale, the failure probability is equal to finding at least one failed elementary volume. We can obtain the final failure probability of the specimen by the weakest link theory again:

$$P_f = 1 - \exp\left(\frac{1}{V_0}\int_{V_p} \ln\left(1 - P(V_0)\right) dV\right) \tag{25}$$

where V_p denotes elementary volumes under plastic deformation.

For fracture toughness predictions, finite element simulations were performed on CT12.5 specimens with side grooves. Only one-quarter of the specimen is meshed thanks to its two planes of symmetry. The refined region around the crack tip is constructed with three-dimensional brick elements having 20 nodes (CU20 in CAST3M). The size is 50 μm×50 μm in the plane normal to the crack surface. 12 layers of elements were built in the thickness direction. One average stress tensor is saved for each element which will be used as the stress condition applied on the boundaries of the elementary volume $\left\langle \sigma_{V_0 I} \right\rangle$.

The parameters for the MIBF model are summarized in Table 5. The analysis for carbide size distribution has been introduced in [21]. The same sets of the 3 parameters α_{carb}, β_{carb} and γ_{carb} related to the carbide size distributions are used in the current paper. Usually, γ_f could be adjusted by fitting K_{Jc}-probability curves at different temperatures [17]. Due to the limitation of available experimental data in the current study, γ_f was obtained by fitting the 50% failure iso-probability curve with the experimental median values of K_{Jc}. These experimental median values used for calibration are taken near the reference temperature as marked with red dots in Fig. 17. It can be noticed that most experimental data points are covered by the 1%–99% iso-probability envelope produced by MIBF model. The predicted results are similar to previous ones (see [21] Fig. 7) without considering the actual crystallographic influence on the local stress distribution. In addition, the stress distribution obtained from current crystal plasticity simulations based on actual material microstructures does not change the scattering range. However, the difference of the γ_f values of the three materials has been significantly reduced. According to experimental observations, the reference temperature T_0 increases with higher segregation level ($T_0 = -123\,°C$ for 0.18%C, $T_0 = -75\,°C$ for 0.29%C). However, for 0.38%C material, the $T_0 = -75\,°C$ is the same as 0.29%C material and does not continue to increase. That is to say the harmfulness of segregation is reduced in the case of 0.38%C. In [21], the reduced harmfulness of 0.38%C material was interpreted by a much larger γ_f value which counterbalances the effect of the increase of number and size of carbides. As shown in Fig. 16, the current stress distributions obtained from crystal plasticity model are less heterogeneous than that used in our previous work. With other parameters unchanged, this results in the shift of T_0 to a lower temperature. The reduced harmfulness observed in 0.38%C could be partially attributed to microstructural evolution. It should also be pointed out that the increased quantity of microstructural barriers from these refined microstructures in 0.38%C material could also prevent the propagation of crack initiators which is not taken into account in MIBF model yet which may have an effect on the value of γ_f.

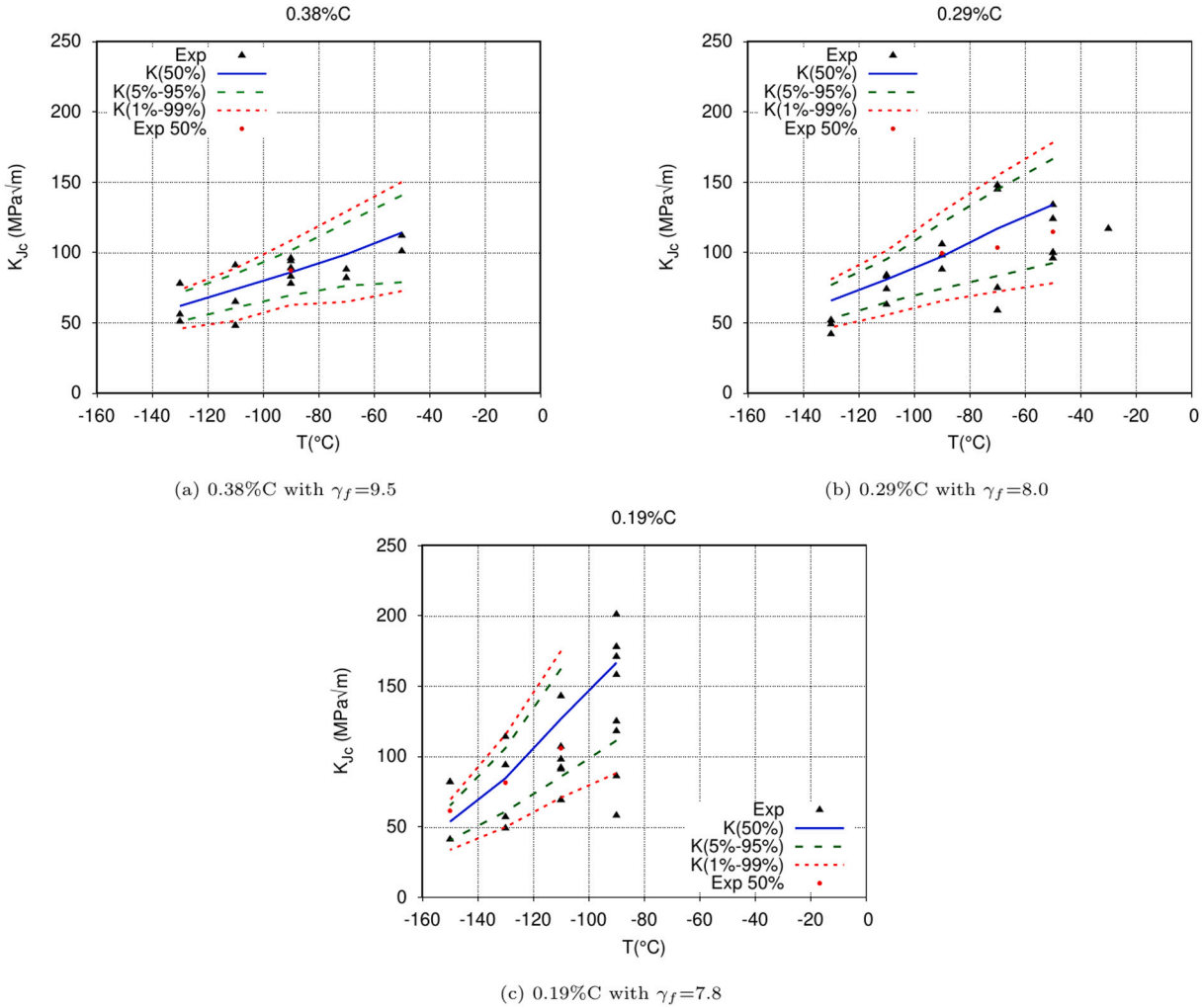

(a) 0.38%C with γ_f=9.5

(b) 0.29%C with γ_f=8.0

(c) 0.19%C with γ_f=7.8

Fig. 17. Experimental fracture toughness results compared with the failure iso-probability envelops predicted by MIBF model.

6. Conclusions

The present study demonstrated the full modelling chain for quantitatively evaluating the fracture toughness of synthetic alloys with different carbon contents. The flexibility of MIBF model is shown by taking into account various microstructural features of different materials through crystal plasticity modelling and experimental measurements. The main results of the current work are summarized below:

Mechanical testing and microstructural characterizations showed the influence of carbon and alloy element contents on the tensile properties, fracture toughness and microstructures of the synthetic alloys. The materials with higher carbon contents showed the following characteristics:

- Increased tensile yield strength.
- The brittle-to-ductile transition zone shifts towards higher temperatures. But when the carbon content is higher than 0.29%, the transition temperature no longer increases.
- Heterogeneous micro-segregation was observed. The proportion of micro-segregated zones increases with carbon content. The probability to find large-sized carbides increases with carbon contents.
- A significant refinement of grains in the micro-segregated zones was observed for 0.38% case.

Crystal plasticity simulations were conducted with aggregate microstructures constructed from the EBSD data of these 3 materials. The identification process of a dislocation density based crystal plasticity law accounting for the strengthening effect from carbides is suggested. Special attention has been paid to the refinement of microstructures caused by micro-segregation observed in 0.38%C material. Numerical simulations showed a significant influence of microstructural evolution on local stress distributions.

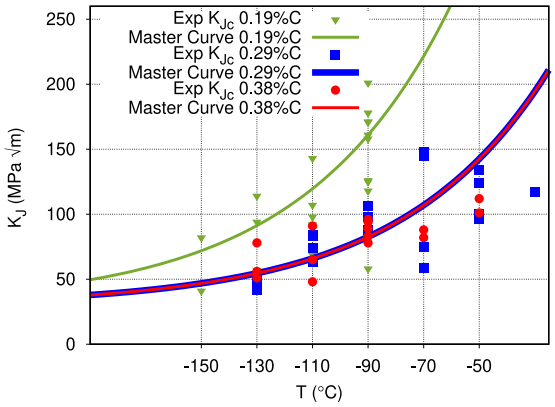

Fig. A.18. Master curves generated using fracture toughness data of these 3 materials according to ASTM E1921.

Both carbide size and local stress distributions based on actual experimental observations are introduced into the MIBF model. The scattering and shifting of fracture toughness results were well captured. The identified values of γ_f for these three materials are closer compared to previous predictions [21] showing the effect of stress heterogeneities in MIBF model. Indeed, the refined microstructure in 0.38%C case provided a source to counterbalance the detrimental effect of carbon increase which explains the saturation of reference temperature shifting. The current modelling work about the different zones observed in 0.38%C material through crystal plasticity is simplified. More detailed work and potential improvement of MIBF model will be carried out in a near future.

CRediT authorship contribution statement

S.C. Ren: Writing – review & editing, Writing – original draft, Visualization, Validation, Software, Methodology, Investigation, Formal analysis, Data curation, Conceptualization. **B. Marini:** Validation, Supervision, Resources, Project administration, Methodology, Investigation, Funding acquisition, Formal analysis, Conceptualization. **P. Forget:** Software, Methodology, Data curation, Conceptualization.

Declaration of competing interest

The authors declare that they have no known competing financial interests or personal relationships that could have appeared to influence the work reported in this paper.

Data availability

Data will be made available on request.

Acknowledgements

This work was initiated and partially funded within the framework of a CEA-EDF-Framatome joint project. The authors want to acknowledge their support related to experimental characterizations and model framework. Special thanks to A. Gangloff (CEA) for EBSD and carbide analysis, E. Pons (CEA) for mechanical testing, C. Toffolon-Masclet (CEA) for Thermalcalc calculations and L. Vincent (CEA) for fruitful discussions about the present results. The authors have also received funding from the EU Euratom Research and Training Programme ENTENTE project [grant number 900018] related to the development of modelling techniques based on measured microstructures and the fracture toughness predictions with MIBF model used in this work.

Appendix. Experimental fracture toughness data and Master curves

Compact tension (CT) specimens with 12.5 mm thickness were extracted from laboratory heats and used for fracture toughness evaluation. The Master curve reference temperature T_0 was determined by the multi-temperature method given by ASTM E1921. K_{Jc} data were censored after surpassing $K_{Jclimit}$ as suggested by Eq. (1) in ASTM E1921–19a. After censoring K_{Jc} and converting the uncensored and censored K_{Jc} to 1T equivalent, the Eq. (20) in E1921–19a was used to determine T_0 with maximum likelihood estimation algorithm. Fig. A.18 gives the Master curves generated using fracture toughness data of these 3 materials.

References

[1] Lefever B, Marie S, Berger T, Bobin Vastra I. Flamanville EPR RPV's Heads carbon segregation: vessel heads manufacturing. In: Pressure vessels and piping conference. Pressure vessels and piping conference, vol. Volume 6A: Materials and fabrication, American Society of Mechanical Engineers; 2018, http://dx.doi.org/10.1115/PVP2018-84492.

[2] Lee S, Kim S, Hwang B, Lee B, Lee C. Effect of carbide distribution on the fracture toughness in the transition temperature region of an SA 508 steel. Acta Mater 2002;50(19):4755–62. http://dx.doi.org/10.1016/S1359-6454(02)00313-0.

[3] Curry DA, Knott JF. Effect of microstructure on cleavage fracture toughness of quenched and tempered steels. Metal Sci 1979;13(6):341–5. http://dx.doi.org/10.1179/msc.1979.13.6.341.

[4] Beremin F, Pineau A, Mudry F, Devaux J-C, D'Escatha Y, Ledermann P. A local criterion for cleavage fracture of a nuclear pressure vessel steel. Metall Mater Trans A 1983;14(11):2277–87. http://dx.doi.org/10.1007/BF02663302.

[5] Pineau A, Benzerga AA, Pardoen T. Failure of metals I: Brittle and ductile fracture. Acta Mater 2016;107:424–83. http://dx.doi.org/10.1016/j.actamat.2015.12.034.

[6] Ruggieri C, Dodds Jr RH. A local approach to cleavage fracture modeling: An overview of progress and challenges for engineering applications. Eng Fract Mech 2018;187:381–403. http://dx.doi.org/10.1016/j.engfracmech.2017.12.021.

[7] Renevey S, Carassou S, Marini B, Eripret C, Pineau A. Ductile-brittle transition of ferritic steels modelled by the local approach to fracture. J Phys IV 1996;6(C6):C6–343. http://dx.doi.org/10.1051/jp4:1996634.

[8] Carassou S, Renevey S, Marini B, Pineau A. Modelling of the ductile to brittle transition of a low alloy steel. In: ECF 12: Fracture from defects, Vol. 2. 1998, p. 691–6.

[9] Mäntylä M, Rossoll A, Nedbal I, Prioul C, Marini B. Fractographic observations of cleavage fracture initiation in a bainitic A508 steel. J Nucl Mater 1999;264(3):257–62. http://dx.doi.org/10.1016/S0022-3115(98)00496-6.

[10] Tanguy B, Besson J, Piques R, Pineau A. Ductile to brittle transition of an A508 steel characterized by charpy impact test: Part I: Experimental results. Eng Fract Mech 2005;72(1):49–72. http://dx.doi.org/10.1016/j.engfracmech.2004.03.010.

[11] Haušild P, Berdin C, Bompard P. Prediction of cleavage fracture for a low-alloy steel in the ductile-to-brittle transition temperature range. Mater Sci Eng A 2005;391(1):188–97. http://dx.doi.org/10.1016/j.msea.2004.08.067.

[12] Chen J, Cao R. Micromechanism of cleavage fracture of metals: A comprehensive microphysical model for cleavage cracking in metals. Butterworth-Heinemann; 2014.

[13] Vincent L, Gélébart L, Dakhlaoui R, Marini B. Stress localization in BCC polycrystals and its implications on the probability of brittle fracture. Mater Sci Eng A 2011;528(18):5861–70. http://dx.doi.org/10.1016/j.msea.2011.04.003.

[14] Libert M, Rey C, Vincent L, Marini B. Temperature dependant polycrystal model application to bainitic steel behavior under tri-axial loading in the ductile–brittle transition. Int J Solids Struct 2011;48(14):2196–208. http://dx.doi.org/10.1016/j.ijsolstr.2011.03.026.

[15] N'Guyen C, Barbe F, Osipov N, Cailletaud G, Marini B, Petry C. Micromechanical local approach to brittle failure in bainite high resolution polycrystals: A short presentation. Comput Mater Sci 2012;64:62–5. http://dx.doi.org/10.1016/j.commatsci.2012.03.034.

[16] Mathieu J-P, Inal K, Berveiller S, Diard O. A micromechanical interpretation of the temperature dependence of Beremin model parameters for french RPV steel. J Nucl Mater 2010;406(1):97–112. http://dx.doi.org/10.1016/j.jnucmat.2010.02.025.

[17] Forget P, Marini B, Vincent L. Application of local approach to fracture of an RPV steel: effect of the crystal plasticity on the critical carbide size. Procedia Struct Integr 2016;2:1660–7. http://dx.doi.org/10.1016/j.prostr.2016.06.210.

[18] Laukkanen A, Uusikallio S, Lindroos M, Andersson T, Kömi J, Porter D. Micromechanics driven design of ferritic–austenitic duplex stainless steel microstructures for improved cleavage fracture toughness. Eng Fract Mech 2021;253:107878. http://dx.doi.org/10.1016/j.engfracmech.2021.107878.

[19] Monnet G, Vincent L, Gélébart L. Multiscale modeling of crystal plasticity in reactor pressure vessel steels: Prediction of irradiation hardening. J Nucl Mater 2019;514:128–38. http://dx.doi.org/10.1016/j.jnucmat.2018.11.028.

[20] Brimbal D. Private communication. Tech. rep., Framatome; 2017.

[21] Ren S, Marini B, Joly P, Todeschini P. Microstructure-informed modelling of the fracture toughness of alloys representing macro-segregated zones in heavy forgings. Procedia Struct Integr 2020;28:684–92. http://dx.doi.org/10.1016/j.prostr.2020.10.079.

[22] Morito S, Tanaka H, Konishi R, Furuhara T, Maki T. The morphology and crystallography of lath martensite in Fe-C alloys. Acta Mater 2003;51(6):1789–99. http://dx.doi.org/10.1016/S1359-6454(02)00577-3.

[23] ASTM E1921-19a. ASTM E1921-19a: Standard test method for determination of reference temperature, T_0, for ferritic steels in the transition range. Standard, West Conshohocken, PA: ASTM International; 2019.

[24] Mandel J. Equations constitutives et directeurs dans les milieux plastiques et viscoplastiques. Int J Solids Struct 1973;9(6):725–40. http://dx.doi.org/10.1016/0020-7683(73)90120-0.

[25] Sabnis PA, Forest S, Arakere NK, Yastrebov VA. Crystal plasticity analysis of cylindrical indentation on a Ni-base single crystal superalloy. Int J Plast 2013;51:200–17. http://dx.doi.org/10.1016/j.ijplas.2013.05.004.

[26] Asaro R, Needleman A. Overview no. 42 Texture development and strain hardening in rate dependent polycrystals. Acta Metall 1985;33(6):923–53. http://dx.doi.org/10.1016/0001-6160(85)90188-9.

[27] Quey R, Dawson P, Barbe F. Large-scale 3D random polycrystals for the finite element method: Generation, meshing and remeshing. Comput Methods Appl Mech Engrg 2011;200(17):1729–45. http://dx.doi.org/10.1016/j.cma.2011.01.002.

[28] Gélébart L, Mondon-Cancel R. Non-linear extension of FFT-based methods accelerated by conjugate gradients to evaluate the mechanical behavior of composite materials. Comput Mater Sci 2013;77:430–9. http://dx.doi.org/10.1016/j.commatsci.2013.04.046.

[29] Pineau A. Development of the local approach to fracture over the past 25 years: Theory and applications. In: Carpinteri A, Mai Y-W, Ritchie RO, editors. Advances in fracture research. Dordrecht: Springer Netherlands; 2006, p. 139–66. http://dx.doi.org/10.1007/978-1-4020-5423-5_9.